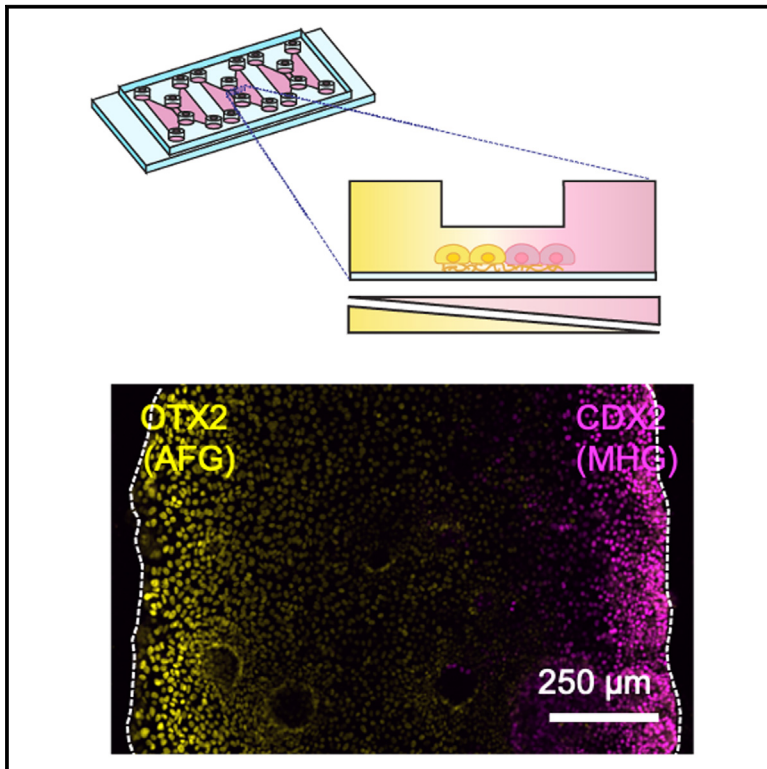


A microfluidic platform for anterior-posterior human endoderm patterning via countervailing morphogen gradients *in vitro*

Graphical abstract



Authors

Leeya Engel, Kevin J. Liu, Kiara W. Cui, ..., Kyle M. Loh, Lay Teng Ang, Alexander R. Dunn

Correspondence

layteng@stanford.edu (L.T.A.), alex.dunn@stanford.edu (A.R.D.)

In brief

Cell biology; Developmental biology; Fluidics; Methodology in biological sciences; Stem cells research

Highlights

- A microfluidic device was used to create opposing morphogen gradients
- HPSC-derived anterior and posterior endoderm were spatially patterned *in vitro*
- Noise in fate decisions was quantitatively assessed using information theory
- Synthetic signaling gradients complement organoid models of tissue patterning



Article

A microfluidic platform for anterior-posterior human endoderm patterning via countervailing morphogen gradients *in vitro*

Leeya Engel,^{1,2} Kevin J. Liu,^{3,7} Kiara W. Cui,^{1,7} Eva L. de la Serna,¹ Vipul T. Vachharajani,^{1,4} Carolyn E. Dundes,^{3,5} Sherry Li Zheng,^{3,5} Manali Begur,³ Kyle M. Loh,^{3,5} Lay Teng Ang,^{3,6,*} and Alexander R. Dunn^{1,8,*}

¹Department of Chemical Engineering, Stanford University, Stanford, CA 94305, USA

²Faculty of Mechanical Engineering, Technion – Israel Institute of Technology, Haifa 3200003, Israel

³Institute for Stem Cell Biology & Regenerative Medicine, Stanford University, Stanford, CA 94305, USA

⁴Program in Biophysics, Medical Scientist Training Program, Stanford University, Stanford, CA 94305, USA

⁵Department of Developmental Biology, Stanford University, Stanford, CA 94305, USA

⁶Department of Urology, Stanford University, Stanford, CA 94305, USA

⁷These authors contributed equally

⁸Lead contact

*Correspondence: layteng@stanford.edu (L.T.A.), alex.dunn@stanford.edu (A.R.D.)

<https://doi.org/10.1016/j.isci.2025.111744>

SUMMARY

Understanding how morphogen gradients spatially pattern tissues is a fundamental question in developmental biology but can be difficult to directly address using conventional approaches. Here, we expose hPSC-derived endoderm cells to countervailing gradients of anteriorizing and posteriorizing signals using a widely available microfluidic device. This approach yielded spatially patterned cultures comprising anterior foregut (precursor to the thyroid, esophagus, and lungs) and mid/hindgut (precursor to the intestines) cells, whose identities were confirmed using single-cell RNA sequencing (scRNA-seq). By exposing stem cells to externally applied signaling gradients, this widely accessible microfluidic platform should accelerate the production of spatially patterned tissues, complementing internally self-organizing organoids. Applying artificial morphogen gradients *in vitro* may also illuminate how developing tissues interpret signaling gradients in systems that are not readily accessible for *in vivo* studies.

INTRODUCTION

During embryonic development, stem cells are exposed to spatial gradients of extracellular signaling molecules known as morphogens. These cells subsequently differentiate into different cell types based on the morphogen concentration to give rise to spatially patterned tissues comprising multiple cell types.^{1–5} Morphogens are, in turn, produced by specialized cell populations known as organizers or signaling centers. The reproducible emergence of spatially patterned tissues *in vivo* is one of the most remarkable aspects of developmental biology, yet many questions remain. What is the relative importance of various input signals? How do cells interpret graded levels of a given signal? Finally, it is becoming increasingly appreciated that the response of individual cells to signaling gradients might be “noisy”, yet what is the degree of noise and how do precisely patterned tissues nonetheless emerge *in vivo*?^{6,7}

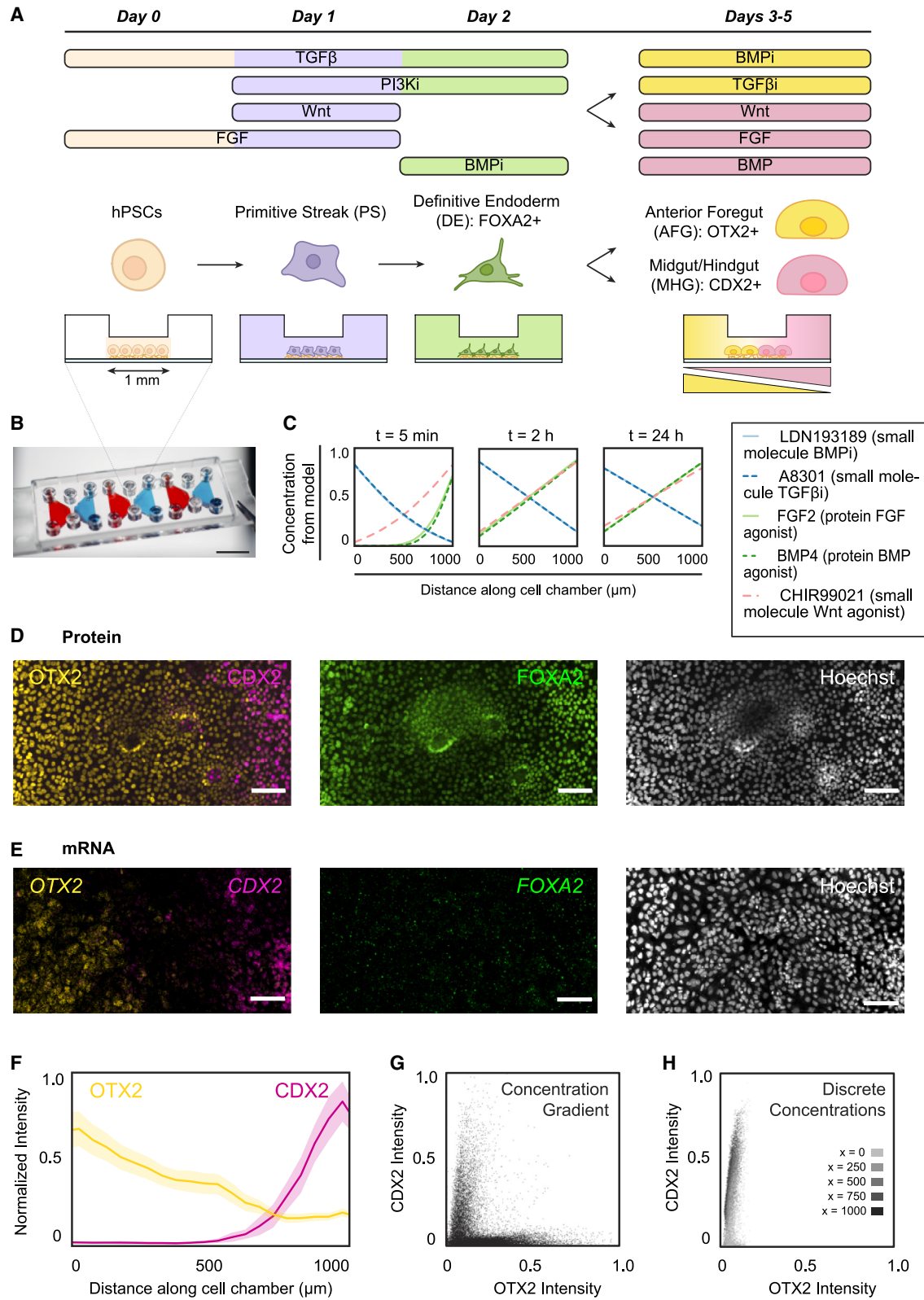
Creating spatially patterned tissues *in vitro* remains a challenge. Remarkably, three-dimensional (3D) cultures of certain cell types will spontaneously self-organize to approximate spatially patterned tissues.^{8–14} In multiple cases, the intrinsic ability of certain organoids to self-organize *in vitro* has been linked to the emergence of cellular signaling centers that create signaling gra-

dients (e.g., BMP or WNT) within the organoid.^{8,15,16} However, not all tissues can extensively self-organize *in vitro*. Many developing tissues *in vivo* (e.g., endoderm, somites, and neural tube) are instead patterned by signaling gradients produced by organizers located outside of the tissue. Spatial patterning of these tissues *in vitro* would thus critically depend on applying an external signaling gradient.

Microfluidic devices have recently been employed to artificially create signaling gradients *in vitro*.¹⁷ The identity and combinations of signals within the gradient, together with the gradient length and steepness, can be theoretically tailored *in vitro*, yet all these parameters would be difficult to finely tune *in vivo*. Pioneering efforts developed custom microfluidic devices to apply signaling gradients to differentiating pluripotent stem cells, thereby generating spatially patterned cultures containing neural^{18–20} or primitive streak cells.²¹ However, these strategies entailed the manufacture of custom microfluidic devices, which might be challenging for stem cell and developmental biology labs to access.

Here, we developed a protocol to apply two opposing signaling gradients across cell populations *in vitro* using a widely available, disposable microfluidic device that does not require external specialized hardware such as fluidic pumping systems. We





(legend on next page)

focused on the endoderm germ layer, which undergoes anterior-posterior patterning *in vivo* to generate the anterior foregut (AFG, precursor to endodermal organs near the head, including the lungs and thyroid) and the posteriorly located mid/hindgut (MHG, which gives rise to the intestinal epithelium).^{22–24} After differentiating human pluripotent stem cells (hPSCs) into primitive streak and definitive endoderm,²⁵ we exposed the endoderm to opposing gradients of anteriorizing and posteriorizing signals emanating from opposite sides of the microfluidic device. Doing so generated spatially patterned cultures of AFG and MHG cells, with transcriptional profiles consistent with those of the developing endoderm *in vivo*. This *in vitro* model enabled us to mechanistically interrogate early anterior-posterior patterning of the developing human endoderm, a topic that is otherwise difficult to access experimentally. Analysis of cell populations exposed to uniform morphogen concentrations, replicating five specific regions along the gradient, highlighted differences in how endoderm cells respond to a morphogen gradient vs. absolute local morphogen concentration. Finally, we applied information theory to establish that most of the information transmitted by the signaling gradients to differentiating endoderm cells in our system is accounted for by a binary AFG or MHG fate decision. More broadly, this widely accessible microfluidic platform for creating artificial morphogen gradients will expand the stem cell and developmental biologist's toolkit.

RESULTS

A microfluidic platform models anterior-posterior endoderm patterning

We developed a protocol that employs microfluidics to establish and maintain opposing morphogen gradients across hPSC-derived endoderm populations over multiple days, enabling simultaneous, regionalized anterior and posterior endoderm induction within the same sheet of cells (Figures 1 and S1A). To make this approach broadly accessible, we employed a commercially available microfluidic device (Ibidi treat μ -slide chemotaxis chamber), which contains a cell culture channel flanked on either end by larger triangular reservoirs (Figure 1B). These two reservoirs are filled with media containing morphogens, which form a gradient across the central cell culture channel (Figures 1B, 1C, S4B, and S4C). We modeled the behavior of

morphogen gradients in the microfluidic devices using numerical simulations, showing that a linear morphogen gradient is established in the cell culture channel via passive diffusion within ~ 2 h and remains stable over the course of 24 h (Figure 1C). Modeling of this sort is quantitative and predictive in the physical circumstances studied here.²⁶ Cellular consumption of growth factors, however, could yield deviations from linear gradients in the concentration distribution of these species (see Reaction Diffusion Modeling in supplemental information). We also experimentally validated the ability of the microfluidics to establish a linear gradient within 2 h and maintain a linear gradient for 24 h using fluorescein (Figures S4B and S4C), a result that is consistent with a prior characterization of the same device.²⁷ Thus, the microfluidic device is compatible with daily media changes as required by a variety of hPSC differentiation protocols.

To pattern the endoderm along the anterior-posterior axis *in vitro* using morphogen gradients, we sequentially differentiated hPSCs within the device into primitive streak and definitive endoderm in one and two days, respectively^{25,28} (Figures 1A and S1B). We next exposed the resulting hPSC-derived endoderm to opposing gradients of anteriorizing signals (TGF β and BMP inhibitors^{25,29}) and posteriorizing signals (BMP, FGF, and WNT agonists^{25,30}) emanating from opposite sides of the microfluidic device. *In vivo*, BMP, FGF and WNT ligands are expressed near the posterior endoderm,^{31–33} observations that provide the rationale for why we use agonists for these pathway as part of our posteriorizing signaling gradient.

Immunofluorescence microscopy and fluorescence *in situ* hybridization revealed that hPSC-derived endoderm underwent spatial patterning to generate AFG- and MHG-like cells at opposite sides of the device. First, the general endodermal marker *FOXA2*³⁴ was expressed across the entire length of the endodermal cell sheet, indicating successful endoderm differentiation (Figures 1D–1F, S1C, and S1D). We tracked *OTX2* and *CDX2* expression to determine AFG and MHG formation because these markers are known to be respectively expressed in AFG^{35,36} and MHG³⁷ *in vivo*. Cells positive for the AFG marker, were localized to one side (left) of the cell sheet, while cells positive for the MHG marker *CDX2* were localized to the opposite side (right) of the endoderm cell sheet, both at the protein and mRNA levels; this was reproducibly observed across 16 experiments

Figure 1. A microfluidic platform models anterior-posterior endoderm patterning

- (A) Overview of morphogen signals used to direct hPSC differentiation into anterior foregut (AFG) and midgut/hindgut (MHG) over the course of six days, with schematics depicting cross-sections of the microfluidic device corresponding to three stages of stem cell differentiation. *FOXA2* expression indicates definitive endoderm, *OTX2* expression indicates anterior foregut, and *CDX2* expression indicates mid/hindgut.
- (B) Photo of a microfluidic device with side reservoirs filled with red and blue food coloring. Cells are seeded into the central cell culture channel. Scale bar, 1 cm.
- (C) Dynamics of concentration gradients in the cell channel of microfluidic devices over the course of 24 h, as modeled using finite element analysis (COMSOL). Blue lines represent small molecule morphogens (TGF β A8301, BMPi LDN193189) with the left reservoir as source. Green lines represent protein morphogens (FGF2, BMP4) with the right reservoir as source, and the pink line represents small molecule morphogens (Wnt, CHIR99021) with the right reservoir as source.
- (D) Representative image of protein-level immunostaining for *OTX2*, *CDX2*, and *FOXA2*, showing localized AFG and MHG populations and *FOXA2* staining throughout. Scale bar, 100 μ m.
- (E) Representative image of mRNA *in situ* hybridization, showing *OTX2* and *CDX2* mRNA transcripts localized to their respective morphogen sources and *FOXA2* transcripts present throughout. Scale bar, 100 μ m.
- (F) Average *OTX2* and *CDX2* intensities (protein-level) as a function of distance across the cell culture channel in the patterned cultures. Intensity is normalized to Hoechst and the highest level of cell expression; $N = 15$ across 3 biological replicates, error bar = SEM.
- (G) Scatterplot showing protein-level *CDX2* vs. *OTX2* intensity for every cell in the patterned cultures.
- (H) Overlapping scatterplots showing *CDX2* vs. *OTX2* intensity for every cell exposed to uniform discrete morphogen concentrations that replicate those found at specific positions within the cell culture channel ($x = 0, 250, 500, 750, 1000 \mu$ m).

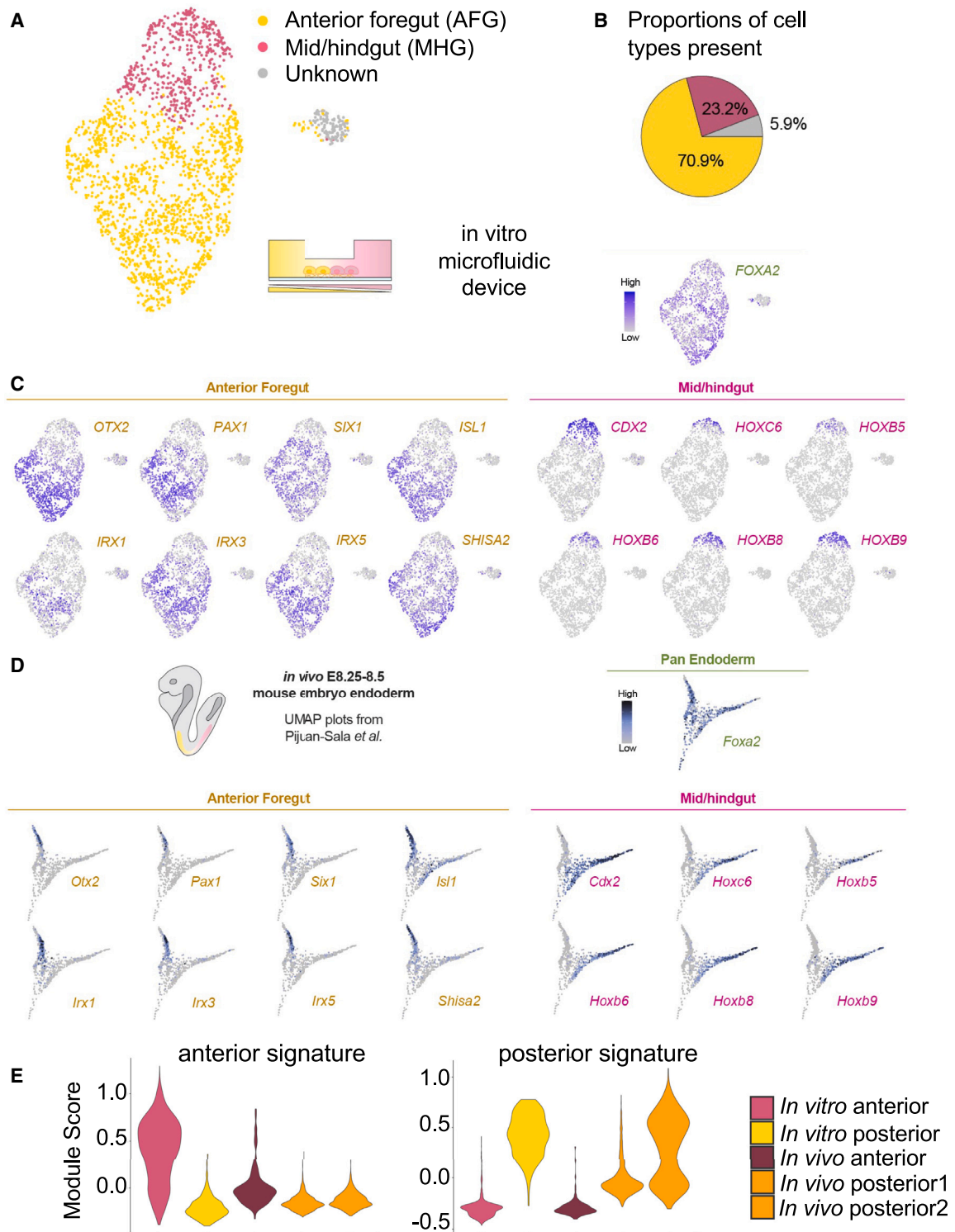


Figure 2. Single-cell RNA sequencing confirms cellular identities present in the patterned endoderm

(A) UMAP plot showing AFG and MHG cell populations in yellow and pink, respectively. Unknown cells are labeled in gray.

(B) Proportions of the different cell types recovered from the devices post-patterning.

(C) UMAP plots of cells recovered from microfluidic devices post-patterning show upregulated genes consistent with pan endoderm and AFG or MHG gene expression profiles *in vivo*.

(legend continued on next page)

(Figures 1D–1F). Both markers showed a decrease in average intensity starting from either edge of the device, suggesting that the two opposing signaling gradients were sufficient to emulate early anterior-posterior patterning of the human endoderm.

In principle, endodermal cells might respond to the local, absolute concentrations of signaling factors, the gradient in signaling factors, or both. To investigate this process, we exposed hPSC-derived endoderm to various uniform media concentrations lacking concentration gradients (mixed AFG- and MHG-inducing conditions in various ratios) that mimicked specific morphogen concentrations at five different positions ($x = 0, 250, 500, 750, 1000 \mu\text{m}$) across the cell culture channel (Figures 1C and S1E). While CDX2 expression scaled with MHG media concentration, there was no discernable OTX2 expression at any uniform media concentration containing AFG and MHG media components (Figures 1G, 1H, and S1E). AFG media alone produced cells with high and uniform expression of OTX2, as expected (Figures S1D and S1E). Microfluidic devices containing a single gradient of AFG media components, without MHG media components, also produced cells with a uniform expression of OTX2 (and without expression of CDX2) (Figure S4A). This finding suggests that graded expression in OTX2 results from the repression of OTX2 in regions with sufficiently high concentrations of MHG media components. This mirrors how posteriorizing endodermal signals repress the expression of anterior endoderm markers *in vivo*.²²

Single-cell RNA sequencing of *in vitro* patterned anterior and posterior endoderm captures cellular diversity

To more comprehensively assess the identity of cells that arose in our endodermal anterior-posterior patterning system, and to expand beyond the use of selected markers (e.g., OTX2 and CDX2), we performed scRNA-seq³⁸ (Figures 2A, 2B, and S2A–S2D). This high-resolution analysis revealed three principal cell-types (Figures 2A and 2B). hPSC-derived AFG populations expressed OTX2, PAX1, SIX1, IRX1, IRX3, IRX5, and SHISA2 (Figures 2C and S7B). We found all of these markers were similarly expressed in AFG within the mouse embryo, as assessed by scRNA-seq³⁹ (Figure 2D). *In situ* staining further confirmed that *Otx2* is expressed in the AFG *in vivo* (Figure S7A).³⁶

hPSC-derived MHG populations were identified by their expression of the posterior marker CDX2 (Figures S2D and S7B); *Cdx2* is expressed in the MHG *in vivo* as evinced by *in situ* staining (Figure S7A).³⁷ hPSC-derived MHG also expressed a panel of HOX genes (i.e., HOXC6, HOXB5, HOXB6, HOXB8, and HOXB9) (Figures 2C and S2D), reiterating its posterior character as *Hox* genes are collinearly expressed along the endodermal anterior-posterior axis *in vivo*.^{24,44} We confirmed that MHG within the mouse embryo³⁹ similarly expressed *Cdx2* and these *Hox* genes (Figure 2D). Expression of FOXA2 confirmed the endodermal nature of both the hPSC-derived AFG and MHG populations (Figure S2D).

In addition to the two main populations of hPSC-derived AFG and MHG endoderm, we also observed a minor cell population of unknown identity (UI) (Figure 2A). This population likely corresponds to the small fraction of cells located by the inlets and outlets of the cell culture channel that were not exposed to morphogen gradients but were recovered from the microfluidic devices along with the target cell populations during cell extraction (Figure S2E). Nevertheless, scoring the hPSC-derived AFG and MHG cells using prevailing AFG and MHG marker signatures^{35,43} showed that our *in vitro* AFG scored similarly to *in vivo* anterior endoderm rather than *in vivo* posterior endoderm (Figure 2E).

scRNA-seq lends support to the hypothesis that anterior (AFG) and posterior (MHG) endoderm respectively responded to the signaling modulators present within the anteriorizing and posteriorizing signaling gradients (Figure 3A). Specifically, posterior endoderm cells responded to the BMP, FGF and WNT agonists within the posteriorizing signaling gradient: posterior endoderm expressed FGF pathway target genes (*IL17RD/SEF*, *SPRY2/4*, *DUSP5/6*) (Figure 3B), WNT pathway target genes (*LGR5*, *SP8*, *LEF1*, *AXIN2*) (Figure 3C), and BMP pathway target genes (*ID1/2/3/4*) (Figure 3D). In contrast, anterior endoderm minimally expressed these pathway target genes (Figures 3B–3D), consistent with the idea that the artificial anteriorizing signaling gradient limits the range of these posteriorizing signals *in vitro*. These signaling pathway target genes showed similar expression within anterior-posteriorly patterned endoderm *in vivo* (Figures S3A–S3C), as shown by scRNA-seq.³⁹

scRNA-seq data likewise allowed us to probe the idea that extracellular signals might upregulate their own expression; this positive autoregulation loop stabilizes signaling gradients and assures robust developmental patterning *in vivo*.⁴⁵ Intriguingly, posterior endoderm cells (which were treated with exogenous FGF and WNT agonists) also endogenously expressed FGF ligands *FGF9* and *FGF17*, as well as WNT ligand *WNT5A* (Figures 3B and 3C). We speculate that expression of these endogenous FGF and WNT ligands within posterior endoderm *in vitro* may help reinforce anterior-posterior patterning *in vitro*. However, it is unclear whether the several pathways that are being enforced simultaneously self-enforce or enforce one another.

In sum, this scRNA-seq analysis supports the emergence of cells with essential similarities to anterior and posterior endoderm within our microfluidic device. The single cell transcriptional profiles of early human anterior and posterior endoderm provide a resource for future studies (see https://anglab.shinyapps.io/anglab_endoderm and Data S1).

Endoderm cells decode position with close to the minimum accuracy necessary to specify a binary fate decision

The imposition of artificial morphogen gradients can in principle provide a means of inferring how cells convert external *inputs* into cell fate decision *outputs* that underlie tissue patterning.

(D) UMAP plots of scRNA-seq data from a published dataset³⁹ showing gene expression profiles of endoderm cells *in vivo* within the E8.25–E8.5 mouse embryo. In particular, *Isl1* is expressed in both foregut and hindgut endoderm *in vivo*.^{40–42}

(E) Comparison of average scores for our *in vitro* human gut endoderm cells with previously published *in vivo* mouse E8.75 anterior and posterior endoderm using AFG and MHG marker signatures (left: AFG; right: MHG).^{35,43} Mouse MHG cells yield two clusters (*in vivo* posterior1, *in vivo* posterior2) with different posterior *Hox* gene expression levels, but both express CDX2.

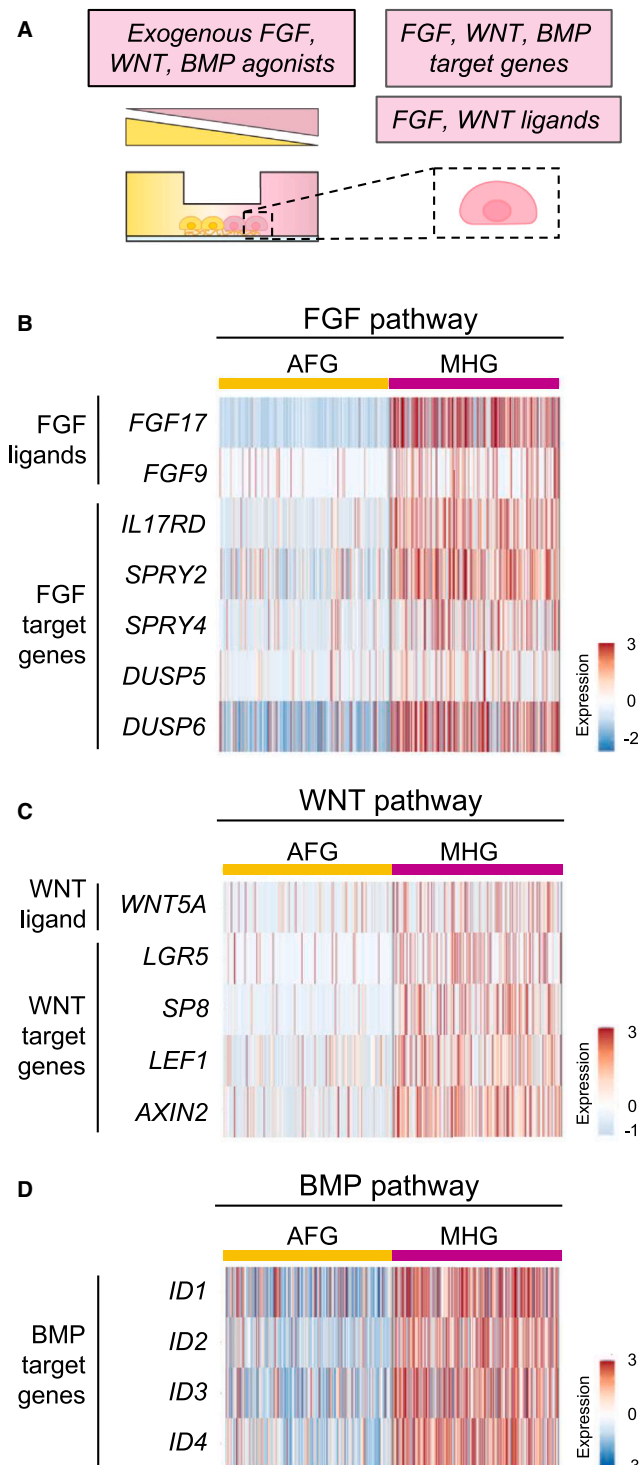


Figure 3. Single-cell RNA sequencing confirms expression of ligands and pathway target genes

(A) Schematic depicting upregulation of expected target genes and ligands in mid/hindgut (MHG) cells resulting from exposure of definitive endoderm to MHG media from the right reservoir.

(B) Heatmap showing upregulation of FGF ligands and target genes in MHG cells and downregulation in anterior foregut (AFG) cells.

We applied an information theory framework to understand the fidelity with which individual definitive endoderm cells exposed to the two opposing morphogen gradients make the AFG or MHG fate decision. Here, we treat the cell mathematically as transforming environmental *inputs* provided by morphogen gradients into cell fate *outputs* as indicated by OTX2 or CDX2 expression (Figure S5A). This operation is intrinsically noisy as a result of the stochastic nature of receptor-ligand binding, signal transduction, and gene expression.⁴⁶ While it is difficult to directly measure the molecular details of signal transduction, it is still possible to make inferences about the fundamental limits of information transmission in the system by observing the noise in the outputs.

To explore this input/output relationship, we first asked how much information about gene expression can be inferred by a cell's position within the gradient. Formally, this value is termed the mutual information and is measured in bits, as is commonly used to quantify information transmission and storage. Importantly, in this framework the information about cell position provided by protein expression is equal to the information about protein expression provided by position (Figure S5B). Thus, mutual information can provide equal insight into the biologically relevant question of how accurately a cell “decodes” its position relative to the morphogen gradients. We computed the mutual information between position within the gradient and OTX2 and/or CDX2 expression, following the framework outlined in Dubuis et al.⁴⁶ (Table S1). Taking OTX2 and CDX2 expression together, we found this value to be 0.89 bits, with CDX2 expression contributing more mutual information (0.77 bits) than OTX2 expression (0.31 bits).

We next investigated how positional information varied in space across the micropatterned culture. More precisely, we asked how accurately a cell's position within the gradient can be inferred from its protein-level expression of OTX2 and CDX2 (Figure S5C). As described previously, this inference can be visualized using a “decoding map,” which depicts the conditional probability of inferring an implied position x^* for a cell at true position x , given only its OTX2 and/or CDX2 expression level.⁴⁷ The more accurately the gene expression level reflects the true position, the tighter the distribution will be along the diagonal $x^* = x$ (Figure S5C). In our system, the OTX2 expression level alone was sufficient to infer position with higher relative accuracy near the left and right edges (Figure S5D). CDX2 expression level alone displayed the greatest contribution to positional inference in its region of graded expression, as indicated by the unimodal ridge along the diagonal between approximately $x = 500 \mu\text{m}$ and $x = 1000 \mu\text{m}$ (Figure S5E). When OTX2 and CDX2 expression levels are taken together, the decoding map distribution tightens along the diagonal only slightly, though the addition of OTX2 expression levels increases predictive capability near $x = 0$ relative to CDX2 alone (Figure S5F).

The mutual information and decoding maps depend on both the cell-intrinsic decoding of morphogen signals and the

(C) Heatmap showing upregulation of WNT ligands and target genes in MHG cells and downregulation in AFG cells.

(D) Heatmap showing upregulation of BMP target genes in MHG cells and downregulation in AFG cells.

cell-extrinsic gradient of morphogens (Figure S5G). For example, a sharp, step-like signaling gradient would likely generate a more defined boundary between AFG and MHG cells, while a less step-like morphogen gradient would specify cell fates in the middle of the channel less precisely (Figure S6). Because the precise profile of the morphogen gradient during development is unknown, the mutual information calculated from our data may not represent the actual capacity of the system to specify position. To account for this, we asked what the maximum possible mutual information was in our system. This value can be found by calculating a quantity formally termed the channel capacity.⁴⁸ The channel capacity represents the maximum precision with which a gradient can specify OTX2 and CDX2 expression, subject to empirically determined cell-intrinsic noise (Figure S5G). We computed the full channel capacity of this system to be approximately 1.2 bits (Table S1), with a greater contribution from CDX2 expression than OTX2 expression. In this case, one bit is sufficient to specify two distinct outputs, i.e., AFG or MHG, or equivalently left vs. right side of the microfluidic channel. Importantly, the channel capacity is less than $\log_2(3) = 1.58$ bits, meaning that even in an ideal case there is only enough information to specify two, but not three, distinct states of OTX2 and CDX2 expression.

Several provisos must be considered in interpreting these results: Although their use is supported by prior literature and single-cell sequencing results, OTX2 and CDX2 may be imperfect proxies for cellular identity. In addition, the apparent variability in expression levels of these proteins reflects a combination of cell-intrinsic stochasticity and measurement noise. Our measurements necessarily reflect a single time-point in what is likely to be a complex trajectory at both the level of individual cells and the evolving microtissue. Finally, the chemical signals that we apply here differ from those that occur *in vivo*. Keeping these limitations in mind, it is interesting to note the correspondence between the amount of information the cells apparently harvest from the applied morphogen gradient and the amount necessary to make a binary fate decision (see discussion).

DISCUSSION

Applying synthetic morphogen gradients *in vitro* provides a reductionist system in which to study developmental tissue patterning and can provide new capabilities for human stem cell differentiation.^{18–21,49,50} Here, we use an accessible microfluidic platform to generate an *in vitro* model of the anterior-posterior patterning of the developing human endoderm. We performed a six-day, on-chip hPSC differentiation using two opposing gradients of signaling pathway activators (BMP, FGF, and WNT agonists, to instruct posterior identity) and signaling pathway inhibitors (TGF β and BMP inhibitors, to confer anterior identity). This produced endoderm progenitors that were spatially patterned along a single axis.

Our approach emulates how, in developmental biology, countervailing gradients of a signaling pathway activator versus a signaling pathway inhibitor are often employed to sharpen developmental patterns, as opposed to a single gradient of a signaling pathway activator.^{51,52} We employed the same approach *in vitro*, thus expanding beyond the use of a single gradient of

signaling pathway activators as in previous studies. Under these dual gradients of signaling pathway activators and inhibitors, the resulting transcription factor expression profiles were monotonic, but not linear. We speculate, based on scRNAseq data, that the endogenous expression of signaling pathway ligands may play a role in generating this response. In this way, engineered systems, such as the one presented here, open the possibility of studying how nonlinearity arises in developmental systems through such positive autoregulation mechanisms.

Our platform provides a practical means to expand the developmental and stem cell biologist's toolkit: it uses a low-cost, commercially available microfluidic device that does not require active fluid pumping. This advance should thus allow many groups to readily apply single or antagonistic synthetic morphogen gradients to their own developmental system of interest. Our platform is compatible with retrieval of live cells (allowing scRNA-seq of patterned cell populations) and live imaging.^{53,54} Live imaging of cells as they respond to synthetic morphogen gradients is promising, as cell migration concurrent with differentiation may contribute to sharpening of spatial patterning during development.⁶ Given that the physical principles underlying the creation of the gradients are well understood, we anticipate that our approach can be generalized to customized device geometries that mimic tissues of varying size and shape.^{55,56}

We used our reductionist model of endoderm anterior-posterior patterning to examine fundamental questions about how cells execute fate decisions. It was not initially clear how cells would interpret the information they received from the opposing morphogen gradients. While cells are likely presented with this scenario *in vivo*, it is in general challenging to systematically manipulate these signals in such an environment. In our *in vitro* system, we found that in the absence of a morphogen gradient, OTX2 expression could not be induced when even small concentrations of MHG media components were present (Figure S1E). In contrast, a smooth profile in OTX2 expression was observed in the presence of the opposing signaling pathway within the context of the morphogen gradients (Figures 1G and 1H). This result suggests that, at least in this system, definitive endoderm cells derive additional information from the spatial gradient that is missing in cultures with homogeneous distributions of signaling factors. Whether this is a general phenomenon in other developmental contexts will be an important subject for future investigations, which we anticipate will be facilitated by the technical advances described here.

We used information theory to quantify the information transmitted between the applied morphogen gradients and differentiating definitive endoderm cells. These calculations suggest that in this system, the definitive endoderm cells respond to the applied gradients as precisely as necessary to specify two spatially patterned fates (AFG and MHG), and no more. We note that in other circumstances, greater precision in fate specification is both required and readily achievable. Embryonic epithelial cells in the *Drosophila* embryo, where spatially precise fate specification is essential, extract several bits of information from the relevant morphogen gradients, sufficient to specify fate with a precision comparable to the width of a single cell.⁴⁶ It is interesting to speculate that evolutionary pressure may cause stem cell

populations to achieve only the minimal necessary precision to robustly pattern the relevant tissue.

Limitations of the study

In vivo, most morphogen gradients consist of endogenous protein (e.g. Wnt) and small-molecule (e.g. retinoic acid) signaling molecules. Here, we combine added growth factors and small-molecule signaling pathway activators and inhibitors to create engineered signaling gradients. This choice reflects the fact that the AFG and MHG media, in isolation, yield highly pure populations of the respective cell types.²⁵ It is nevertheless striking that opposing gradients in these media formulations yield, so far as we can determine, AFG- and MHG-like populations rather than a more complex, and less biologically relevant, mixture of cell types. Whether similarly distinct outcomes will occur when analogous synthetic morphogen gradients are used to replicate other tissue patterning events is an important question, both scientifically and practically.

The endoderm germ layer encompasses AFG, posterior foregut (PFG), and MHG *in vivo*,^{22–24} but a PFG-like domain is absent from our present *in vitro* system. *In vivo*, retinoic acid (RA) is produced from multiple sources, including the somites, and RA medializes the endoderm germ layer and induces PFG identity.^{22,23,57} Here, we provided AFG- and MHG-inducing signals from opposite sides, but we did not provide RA at an intermediate position. In the future, one could incorporate PFG-inducing signals (e.g., RA) at an intermediate position within a microfluidic platform, which might open the door to a fully integrated AFG-PFG-MHG endoderm model. This reductionist 2D system could complement more complex 3D PFG models.⁵⁸

In our work, we apply signaling pathway activators vs. signaling pathway inhibitors from different poles of our microfluidic device to spatially pattern endoderm populations. In the developing embryo, certain tissues are patterned by countervailing gradients of different signaling pathway agonists: for instance, the developing spinal cord, BMP is dorsalizing whereas Hedgehog is ventralizing.⁵⁹ Nevertheless, to the best of our knowledge, there is no widely accepted “anteriorizing” signal for the endoderm; rather, anterior endoderm identity is apparently instructed by inhibitors of posteriorizing signals such as BMP, FGF, and WNT *in vivo*.^{22–24} This is in and of itself interesting, implying that absence of a developmental signal in and of itself serves as a signal.⁶⁰

Our study encompasses certain technical limitations. In contrast to the 2D cell culture model used here, most tissues are intrinsically 3D. The microfluidic platform used here can, in principle, apply morphogen gradients across 3D cultures of cells or organoids suspended in a matrix within the cell culture chamber. A related limitation of the commercial microfluidic device used in this study is that the dimensions of the cell culture channel cannot be customized to match those of physiologically relevant length scales. In addition, the degree to which the cell populations observed in this study exactly replicate those present in human development is uncertain owing to a lack of adequate human embryo gene expression data. This provides an interesting avenue for future investigation. The small dimensions of the cell culture channel (1 by 2 mm) can also make it challenging to achieve a sufficiently high number of viable cell colonies after cell seeding, especially if the concentration of the cell suspension

was below a certain threshold. Future studies using conceptually similar passive microfluidic approaches may be helpful in expanding the range of our approach to other tissue sizes and shapes. Finally, the present study focused on replicating two successive differentiation steps, namely the production of definitive endoderm followed by AFG and MHG. Optimization of culture conditions beyond the scope of this study would be required to extend this approach to the production of subsequent cell types or replicate patterning of other types of tissue.

RESOURCE AVAILABILITY

Lead contact

Further information and requests for resources and reagents should be directed to the lead contact, Alexander R. Dunn (alex.dunn@stanford.edu).

Materials availability

This study did not generate new unique reagents.

Data and code availability

- Patterned endoderm single cell RNA-seq data is available through the Gene Expression Omnibus (GEO accession GSE285075): <https://www.ncbi.nlm.nih.gov/geo/query/acc.cgi?acc=GSE285075>.
- A browser containing the single cell RNA-seq data is available at this link: https://anglab.shinyapps.io/anglab_endoderm/.
- Information theory code is available at this link: <https://github.com/AlexDunnLab/endoderm-patterning-2022>.
- All other data reported in the paper are available from the [lead contact](#) upon request.
- Any additional information required to reanalyze the data reported in this paper is available upon request from the [lead contact](#).

ACKNOWLEDGMENTS

We thank A. Elefanty, E. Stanley and E. Ng for *MIXL1-GFP* and *SOX17-mCherry* human pluripotent stem cells (hPSCs) and C. Vasquez, C. Hueschen, C.M. Chai, A. Mukund for discussions. This work was supported by the California Institute for Regenerative Medicine (RB4-06102 [A.R.D.], DISC2-11105 [L.T.A.], DISC-10679 [L.T.A.]), Stanford Maternal and Child Health Research Institute, National Institutes of Health Director’s Early Independence Award DP5OD024558 (K.M.L.), the Juvenile Diabetes Research Foundation (JDRF) Northern California Center of Excellence (KML), Stanford Enhancing Diversity in Graduate Education (EDGE) and Bio-X Bowes Fellowships (K.W.C.), and NIH (T32GM120007 [K.W.C.], T32GM007365 [VTV], and F30DK124985 [V.T.V.]). Infrastructure support was provided by the Stanford Cell Sciences Imaging Facility, Stanford Neuroscience Microscopy Service, Stanford Genomics Service Center, Stanford Stem Cell Fluorescence Activated Cell Sorting (FACS) Core Facility (C. Carswell-Crumpton), and Stanford Diabetes Genomics Analysis Core Facility (NIH P30DK116074). K.M.L. is a Human Frontier Science Program Young Investigator, Packard Foundation Fellow, Pew Scholar, Baxter Foundation Faculty Scholar and The Anthony DiGenova Endowed Faculty Scholar. L.T.A. is a Siebel Investigator and an Additional Ventures Career Development Awardee. L.E. is a Diane and Guilford Glazer Foundation Faculty Fellow.

AUTHOR CONTRIBUTIONS

L.E.: Conceptualization, Methodology, Investigation, Formal Analysis, Writing – Original Draft, Visualization, Project administration. **K.W.C.:** Conceptualization, Methodology, Investigation, Software, Formal Analysis, Writing – Original Draft, Visualization, Project administration. **K.J.L.:** Investigation, Methodology, Software, Writing – Original Draft, Visualization. **E.L.D.:** Methodology, Visualization, Formal Analysis, Writing – Original Draft. **V.T.V.:** Software, Formal Analysis, and Writing – Original Draft. **C.E.D.:** Investigation, Visualization. **S.L.Z.:** Investigation. **M.B.:** Investigation, Resources. **K.M.L.:** Conceptualization, Methodology,

Writing – Review and Editing. **L.T.A.:** Investigation, Conceptualization, Methodology, Software, Writing – Original Draft, Visualization, Supervision, Funding acquisition. **A.R.D.:** Conceptualization, Methodology, Formal Analysis, Software, Writing – Original Draft, Supervision, Funding acquisition.

DECLARATION OF INTERESTS

The authors declare no competing interests.

STAR★METHODS

Detailed methods are provided in the online version of this paper and include the following:

- KEY RESOURCES TABLE
- EXPERIMENTAL MODEL AND STUDY PARTICIPANT DETAILS
 - Human embryonic stem cells
 - Mouse embryos
- METHOD DETAILS
 - Stem cell differentiation into anterior and posterior endoderm
 - RNA extraction, cDNA generation, and qPCR
 - Spatial patterning of stem cell differentiation in microfluidic channels
 - Discrete uniform morphogen concentration experiments
 - Modeling concentration gradient profiles and dynamics
 - *In situ* hybridization chain reaction for detecting mRNA expression
 - *In situ* staining of whole mouse embryos
 - Single cell RNA sequencing (scRNAseq) of spatially patterned cultures
 - Imaging and image analysis
 - Information theory calculations
 - Comparing *in vitro* vs. *in vivo* hepatocytes using single-cell RNA-sequencing
- QUANTIFICATION AND STATISTICAL ANALYSIS
- ADDITIONAL RESOURCES

SUPPLEMENTAL INFORMATION

Supplemental information can be found online at <https://doi.org/10.1016/j.isci.2025.111744>.

Received: March 30, 2024

Revised: September 22, 2024

Accepted: January 2, 2025

Published: January 4, 2025

REFERENCES

1. Stapornwongkul, K.S., and Vincent, J.P. (2021). Generation of extracellular morphogen gradients: the case for diffusion. *Nat. Rev. Genet.* **22**, 393–411.
2. Wolpert, L. (1969). Positional information and the spatial pattern of cellular differentiation. *J. Theor. Biol.* **25**, 1–47.
3. Lander, A.D. (2007). Morpheus Unbound: Reimagining the Morphogen Gradient. *Cell* **128**, 245–256.
4. Green, J.B.A., and Sharpe, J. (2015). Positional information and reaction-diffusion: Two big ideas in developmental biology combine. *Development* **142**, 1203–1211.
5. Rogers, K.W., and Schier, A.F. (2011). Morphogen gradients: From generation to interpretation. *Annu. Rev. Cell Dev. Biol.* **27**, 377–407.
6. Xiong, F., Tentner, A.R., Huang, P., Gelas, A., Mosaliganti, K.R., Souhait, L., Rannou, N., Swinburne, I.A., Obholzer, N.D., Cowgill, P.D., et al. (2013). Specified neural progenitors sort to form sharp domains after noisy Shh signaling. *Cell* **153**, 550–561.
7. Zagorski, M., Tabata, Y., Brandenburg, N., Lutolf, M.P., Tkacik, G., Bollenbach, T., Briscoe, J., and Kicheva, A. (2017). Decoding of position in the developing neural tube from antiparallel morphogen gradients. *Science* **356**, 1379–1383.
8. Sato, T., and Clevers, H. (2013). Growing self-organizing mini-guts from a single intestinal stem cell: Mechanism and applications. *Science* **340**, 1190–1194.
9. Clevers, H. (2016). Modeling Development and Disease with Organoids. *Cell* **165**, 1586–1597.
10. Steinberg, M.S. (1963). Reconstruction of tissues by dissociated cells. *Science* **141**, 401–408.
11. Lancaster, M.A., and Knoblich, J.A. (2014). Organogenesis in a dish: Modeling development and disease using organoid technologies. *Science* **345**, 345.
12. Paşca, S.P. (2018). The rise of three-dimensional human brain cultures. *Nature* **553**, 437–445.
13. Takebe, T., and Wells, J.M. (2019). Organoids by design. *Science* **364**, 956–959.
14. Hofer, M., and Lutolf, M.P. (2021). Engineering organoids. *Nat. Rev. Mater.* **6**, 402–420.
15. Moris, N., Anlas, K., van den Brink, S.C., Alemany, A., Schröder, J., Ghimire, S., Balayo, T., van Oudenaarden, A., and Martinez Arias, A. (2020). An *in vitro* model of early anteroposterior organization during human development. *Nature* **582**, 410–415.
16. ten Berge, D., Koole, W., Fuerer, C., Fish, M., Eroglu, E., and Nusse, R. (2008). Wnt Signaling Mediates Self-Organization and Axis Formation in Embryoid Bodies. *Cell Stem Cell* **3**, 508–518.
17. Sonnen, K.F., and Merten, C.A. (2019). Microfluidics as an Emerging Precision Tool in Developmental Biology. *Dev. Cell* **48**, 293–311.
18. Rifès, P., Isaksson, M., Rathore, G.S., Aldrin-Kirk, P., Möller, O.K., Barzaghi, G., Lee, J., Egerod, K.L., Rausch, D.M., Parmar, M., et al. (2020). Modeling neural tube development by differentiation of human embryonic stem cells in a microfluidic WNT gradient. *Nat. Biotechnol.* **38**, 1265–1273.
19. Demers, C.J., Soundararajan, P., Chennampally, P., Cox, G.A., Briscoe, J., Collins, S.D., and Smith, R.L. (2016). Development-on-chip: *In vitro* neural tube patterning with a microfluidic device. *Development (Camb.)* **143**, 1884–1892.
20. Xue, X., Kim, Y.S., Ponce-Arias, A.I., O’Laughlin, R., Yan, R.Z., Kobayashi, N., Tshuva, R.Y., Tsai, Y.H., Sun, S., Zheng, Y., et al. (2024). A patterned human neural tube model using microfluidic gradients. *Nature* **628**, 391–399.
21. Regier, M.C., Tokar, J.J., Warrick, J.W., Pabon, L., Berthier, E., Beebe, D.J., and Stevens, K.R. (2019). User-defined morphogen patterning for directing human cell fate stratification. *Sci. Rep.* **9**, 6433.
22. Zorn, A.M., and Wells, J.M. (2009). Vertebrate endoderm development and organ formation. *Annu. Rev. Cell Dev. Biol.* **25**, 221–251.
23. Grapin-Botton, A. (2005). Antero-posterior patterning of the vertebrate digestive tract: 40 years after Nicole Le Douarin’s PhD thesis. *Int. J. Dev. Biol.* **49**, 335–347.
24. Grapin-Botton, A., and Melton, D.A. (2000). Endoderm development: From patterning to organogenesis. *Trends Genet.* **16**, 124–130.
25. Loh, K.M., Ang, L.T., Zhang, J., Kumar, V., Ang, J., Auyeong, J.Q., Lee, K.L., Choo, S.H., Lim, C.Y.Y., Nichane, M., et al. (2014). Efficient endoderm induction from human pluripotent stem cells by logically directing signals controlling lineage bifurcations. *Cell Stem Cell* **14**, 237–252.
26. Carvalho, V., Rodrigues, R.O., Lima, R.A., and Teixeira, S. (2021). Computational simulations in advanced microfluidic devices: A review. *Micromachines* **12**, 1149.

27. Zengel, P., Nguyen-Hoang, A., Schildhammer, C., Zantl, R., Kahl, V., and Horn, E. (2011). μ -Slide Chemotaxis: A new chamber for long-term chemotaxis studies. *BMC Cell Biol.* *12*, 1–4.
28. Ang, L.T., Tan, A.K.Y., Autio, M.I., Goh, S.H., Choo, S.H., Lee, K.L., Tan, J., Pan, B., Lee, J.J.H., Lum, J.J., et al. (2018). A Roadmap for Human Liver Differentiation from Pluripotent Stem Cells. *Cell Rep.* *22*, 2190–2205.
29. Green, M.D., Chen, A., Nostro, M.C., d'Souza, S.L., Schaniel, C., Lemischka, I.R., Gouon-Evans, V., Keller, G., and Snoeck, H.W. (2011). Generation of anterior foregut endoderm from human embryonic and induced pluripotent stem cells. *Nat. Biotechnol.* *29*, 267–272.
30. Spence, J.R., Mayhew, C.N., Rankin, S.A., Kuhar, M.F., Vallance, J.E., Tolle, K., Hoskins, E.E., Kalinichenko, V.V., Wells, S.I., Zorn, A.M., et al. (2011). Directed differentiation of human pluripotent stem cells into intestinal tissue in vitro. *Nature* *470*, 105–109.
31. Danesh, S.M., Villasenor, A., Chong, D., Soukup, C., and Cleaver, O. (2009). BMP and BMP receptor expression during murine organogenesis. *Gene Expr. Patterns* *9*, 255–265.
32. Garriock, R.J., Chalamalasetty, R.B., Zhu, J., Kennedy, M.W., Kumar, A., Mackem, S., and Yamaguchi, T.P. (2020). A dorsal-ventral gradient of Wnt3a/ β -catenin signals controls mouse hindgut extension and colon formation. *Development* *147*, dev185108.
33. Crossley, P.H., and Martin, G.R. (1995). The mouse *Fgf8* gene encodes a family of polypeptides and is expressed in regions that direct outgrowth and patterning in the developing embryo. *Development* *121*, 439–451.
34. Sasaki, H., and Hogan, B.L. (1993). Differential expression of multiple fork head related genes during gastrulation and axial pattern formation in the mouse embryo. *Development* *118*, 47–59.
35. Nowotschin, S., Setty, M., Kuo, Y.Y., Liu, V., Garg, V., Sharma, R., Simon, C.S., Saiz, N., Gardner, R., Boutet, S.C., et al. (2019). The emergent landscape of the mouse gut endoderm at single-cell resolution. *Nature* *569*, 361–367.
36. Ang, S.L., Conlon, R.A., Jin, O., and Rossant, J. (1994). Positive and negative signals from mesoderm regulate the expression of mouse *Otx2* in ectoderm explants. *Development* *120*, 2979–2989.
37. Beck, F., Erler, T., Russell, A., and James, R. (1995). Expression of *Cdx-2* in the mouse embryo and placenta: Possible role in patterning of the extra-embryonic membranes. *Dev. Dynam.* *204*, 219–227.
38. Zheng, G.X.Y., Terry, J.M., Belgrader, P., Ryvkin, P., Bent, Z.W., Wilson, R., Ziraldo, S.B., Wheeler, T.D., McDermott, G.P., Zhu, J., et al. (2017). Massively parallel digital transcriptional profiling of single cells. *Nat. Commun.* *8*, 14049.
39. Pijuan-Sala, B., Griffiths, J.A., Guibentif, C., Hiscock, T.W., Jawaid, W., Calero-Nieto, F.J., Mulas, C., Ibarra-Soria, X., Tyser, R.C.V., Ho, D.L.L., et al. (2019). A single-cell molecular map of mouse gastrulation and early organogenesis. *Nature* *566*, 490–495.
40. Kim, E., Jiang, M., Huang, H., Zhang, Y., Tjota, N., Gao, X., Robert, J., Gilmore, N., Gan, L., and Que, J. (2019). *Isl1* Regulation of *Nkx2.1* in the Early Foregut Epithelium Is Required for Trachea-Esophageal Separation and Lung Lobation. *Dev. Cell* *57*, 675–683.
41. Zhuang, S., Zhang, Q., Zhuang, T., Evans, S.M., Liang, X., and Sun, Y. (2013). Expression of *Isl1* during mouse development. *Gene Expr. Patterns* *13*, 407–412.
42. Kappen, C., and Salbaum, J.M. (2009). Identification of regulatory elements in the *Isl1* gene locus. *Int. J. Dev. Biol.* *53*, 935–946.
43. Vianello, S., and Lutolf, M. (2020). In vitro endoderm emergence and self-organisation in the absence of extraembryonic tissues and embryonic architecture. Preprint at bioRxiv. <https://doi.org/10.1101/2020.06.07.138883>.
44. Sherwood, R.I., Chen, T.Y.A., and Melton, D.A. (2009). Transcriptional dynamics of endodermal organ formation. *Dev. Dynam.* *238*, 29–42.
45. Loh, K.M., van Amerongen, R., and Nusse, R. (2016). Generating Cellular Diversity and Spatial Form: Wnt Signaling and the Evolution of Multicellular Animals. *Dev. Cell* *38*, 643–655.
46. Dubuis, J.O., Tkacik, G., Wieschaus, E.F., Gregor, T., and Bialek, W. (2013). Positional information, in bits. *Proc. Natl. Acad. Sci. USA* *110*, 16301–16308.
47. Petkova, M.D., Tkačik, G., Bialek, W., Wieschaus, E.F., and Gregor, T. (2019). Optimal Decoding of Cellular Identities in a Genetic Network. *Cell* *176*, 844–855.
48. Rhee, A., Cheong, R., and Levchenko, A. (2012). The application of information theory to biochemical signaling systems. *Phys. Biol.* *9*, 045011.
49. Manfrin, A., Tabata, Y., Paquet, E.R., Vuaridel, A.R., Rivest, F.R., Naef, F., and Lutolf, M.P. (2019). Engineered signaling centers for the spatially controlled patterning of human pluripotent stem cells. *Nat. Methods* *16*, 640–648.
50. Li, P., Markson, J.S., Wang, S., Chen, S., Vachharajani, V., and Elowitz, M.B. (2018). Morphogen gradient reconstitution reveals Hedgehog pathway design principles. *Science* *360*, 543–548.
51. Bier, E., and De Robertis, E.M. (2015). BMP gradients: A paradigm for morphogen-mediated developmental patterning. *Science* *348*, aaa5838.
52. Barkai, N., and Shilo, B.Z. (2009). Robust generation and decoding of morphogen gradients. *Cold Spring Harbor Perspect. Biol.* *1*, a001990. <https://doi.org/10.1101/cshperspect.a001990>.
53. Zengel, P., Nguyen-Hoang, A., Schildhammer, C., Zantl, R., Kahl, V., and Horn, E. (2011). μ -Slide Chemotaxis: A new chamber for long-term chemotaxis studies. *BMC Cell Biol.* *12*, 21.
54. Cui, K.W., Engel, L., Dundes, C.E., Nguyen, T.C., Loh, K.M., and Dunn, A.R. (2020). Spatially controlled stem cell differentiation via morphogen gradients: A comparison of static and dynamic microfluidic platforms. *J. Vac. Sci. Technol. A* *38*, 033205.
55. Wang, X., Liu, Z., and Pang, Y. (2017). Concentration gradient generation methods based on microfluidic systems. *RSC Adv.* *7*, 29966–29984.
56. Paratore, F., Bacheva, V., Bercovici, M., and Kaigala, G.V. (2022). Reconfigurable microfluidics. *Nat. Rev. Chem* *6*, 70–80. <https://doi.org/10.1038/s41570-021-00343-9>.
57. Shimoazono, S., Iimura, T., Kitaguchi, T., Higashijima, S.I., and Miyawaki, A. (2013). Visualization of an endogenous retinoic acid gradient across embryonic development. *Nature* *496*, 363–366.
58. Koike, H., Iwasawa, K., Ouchi, R., Maezawa, M., Giesbrecht, K., Saiki, N., Ferguson, A., Kimura, M., Thompson, W.L., Wells, J.M., et al. (2019). Modeling human hepato-biliary-pancreatic organogenesis from the foregut-midgut boundary. *Nature* *574*, 112–116.
59. Zagorski, M., Tabata, Y., Brandenburg, N., Lutolf, M.P., Tkačik, G., Bollenbach, T., Briscoe, J., and Kicheva, A. (2017). Decoding of position in the developing neural tube from antiparallel morphogen gradients. *Science* *356*, 1379–1383.
60. Gilbert, S.F. (2008). All I really needed to know I learned during gastrulation. *CBE-Life Sci. Educ.* *7*, 12–13.
61. Thomson, J.A., Itskovitz-Eldor, J., Shapiro, S.S., Waknitz, M.A., Swiergiel, J.J., Marshall, V.S., and Jones, J.M. (1998). Embryonic Stem Cell Lines Derived from Human Blastocysts. *Science* *282*, 1145–1147.
62. International Stem Cell Initiative; Amps, K., Andrews, P.W., Anyfantis, G., Armstrong, L., Avery, S., Baharvand, H., Baker, J., Baker, D., Munoz, M.B., et al. (2011). Screening ethnically diverse human embryonic stem cells identifies a chromosome 20 minimal amplicon conferring growth advantage. *Nat. Biotechnol.* *29*, 1132–1144.
63. Ang, L.T., Nguyen, A.T., Liu, K.J., Chen, A., Xiong, X., Curtis, M., Martin, R.M., Rafferty, B.C., Ng, C.Y., Vogel, U., et al. (2022). Generating human artery and vein cells from pluripotent stem cells highlights the arterial tropism of Nipah and Hendra viruses. *Cell* *185*, 2523–2541.
64. Fischer, H., Polikarpov, I., and Craievich, A.F. (2004). Average protein density is a molecular-weight-dependent function. *Protein Sci.* *13*, 2825–2828.
65. He, L., and Niemeyer, B. (2003). A novel correlation for protein diffusion coefficients based on molecular weight and radius of gyration. *Biotechnol. Prog.* *19*, 544–548.

66. Wang, C., Lu, H., and Schwartz, M.A. (2012). A novel in vitro flow system for changing flow direction on endothelial cells. *J. Biomech.* *45*, 1212–1218.
67. Choi, H.M.T., Schwarzkopf, M., Fornace, M.E., Acharya, A., Artavanis, G., Stegmaier, J., Cunha, A., and Pierce, N.A. (2018). Third-generation in situ hybridization chain reaction: Multiplexed, quantitative, sensitive, versatile, robust. *Development (Camb.)* *145*, dev165753.
68. Stuart, T., Butler, A., Hoffman, P., Hafemeister, C., Papalexi, E., Mauck, W.M., 3rd, Hao, Y., Stoeckius, M., Smibert, P., and Satija, R. (2019). Comprehensive Integration of Single-Cell Data. *Cell* *177*, 1888–1902.
69. Schindelin, J., Arganda-Carreras, I., Frise, E., Kaynig, V., Longair, M., Pietzsch, T., Preibisch, S., Rueden, C., Saalfeld, S., Schmid, B., et al. (2012). Fiji: An open-source platform for biological-image analysis. *Nat. Methods* *9*, 676–682.

STAR★METHODS

KEY RESOURCES TABLE

REAGENT or RESOURCE	SOURCE	IDENTIFIER
Antibodies		
Mouse monoclonal anti-CDX2 antibody	Biogenex	Cat#CDX2-88
Goat polyclonal anti-OTX2 antibody	R&D	Cat#AF1979
Rabbit polyclonal anti-FOXA2 antibody	Millipore	Cat#07-633
Goat polyclonal anti-SOX2 antibody	R&D Systems	Cat#AF2018
Goat anti-rabbit IgG Fragment Alexa Fluor 488 Conjugate	Cell Signaling Technology	Cat#4412
Goat anti-mouse IgG Fragment Alexa Fluor 555 Conjugate	Cell Signaling Technology	Cat#4409S
Goat anti-goat IgG Alexa Fluor 647 Conjugate	Cell Signaling Technology	Cat#4414S
Chemicals, peptides and recombinant proteins		
Hoechst 33342	Thermo Fisher	Cat#62249
Geltrex basement matrix	Thermo Fisher	A1413302
DMEM/F12	Thermo Fisher	10565042
mTeSR Plus	STEMCELL Technologies	05825
Penicillin/streptomycin	Thermo Fisher	15-140-122
Versene	Thermo Fisher	15040066
Deposited data		
Raw data for scRNAseq analysis, see Data S1.	This paper	Data S1.xlsx
Raw data containing a list of unknown cluster's enriched genes, see Data S2.	This paper	Unknown_cluster_genes.xlsx
H1-derived patterned endoderm scRNA-seq data	Gene Expression Omnibus (GEO) records	GSE285075
Experimental models: Cell lines		
H1 human embryonic stem cells (hESCs)	WiCell	WA01
Experimental models: Organisms/strains		
Outbred CD-1 mouse embryos	Charles River Laboratories	Strain 022
Oligonucleotides		
qPCR Primer: <i>YWHAZ</i> Forward: GAGCTGGTTCAGAAGGCCAAAC	This paper	N/A
qPCR Primer: <i>OTX2</i> Forward: GGAAGCACTGTTTGCCAAGACC	This paper	N/A
qPCR Primer: <i>IRX1</i> Forward: GCTCGCAGTATGAACTGAAGG	This paper	N/A
qPCR Primer: <i>PAX1</i> Forward: CGCTATGGAGCAGACGTATGGCGA	This paper	N/A
qPCR Primer: <i>CDX2</i> Forward: GGGCTCTCTGAGAGGCAGGT	This paper	N/A
qPCR Primer: <i>HOXB8</i> Forward: GACCCCGCAATTCTACGG	This paper	N/A
Software and algorithms		
Information theory code	This paper	https://github.com/AlexDunnLab/endoderm-patterning-2022
Browser of single cell RNA-seq data	This paper	https://anglab.shinyapps.io/anglab_endoderm/

EXPERIMENTAL MODEL AND STUDY PARTICIPANT DETAILS

Human embryonic stem cells

H1 human embryonic stem cells (hESCs) were obtained from WiCell (catalog number WA01). H1 hESCs are of Central European ethnicity and are biologically male (XY).^{61,62} Undifferentiated hESCs were cultured as described previously in in standard incubator conditions (20% O₂, 5% CO₂, and 37°C).⁶³ In brief, undifferentiated H1 hESCs were cultured on plastic cell culture dishes that were coated with Geltrex basement matrix (Thermo Fisher, A1413302) in that had been diluted 1:100 in DMEM/F12 (Thermo Fisher,

10565042) for 1 h at 37°C. Cells were maintained in mTeSR Plus (STEMCELL Technologies, 05825) with 1% penicillin/streptomycin (Thermo Fisher, 15-140-122) and media was changed daily. When hESCs were ~80% confluent, they were passaged as aggregates using EDTA (Versene; Thermo Fisher, 15040066) onto new Geltrex-coated plates. All hESC experiments were performed using procedures institutionally approved by the Stanford Stem Cell Research Oversight (SCRO) committee.

Mouse embryos

CD-1 mice were obtained from Charles River Laboratories, and embryonic day 9.5 (E9.5) mouse embryos were collected. Biological sex of mouse embryos was not explicitly considered in this study, because there are no known major differences in early endoderm germ layer development that are driven by biological sex. All mouse experiments were performed using procedures institutionally approved by the Stanford Administrative Panel on Laboratory Animal Care (APLAC).

METHOD DETAILS

Stem cell differentiation into anterior and posterior endoderm

Prior to cell seeding, 12-well plastic tissue culture plates were coated with Geltrex as described above. H1 hESCs were dissociated into single cells using TrypLE Express and seeded at a density of 150,000 cells per well in mTESR Plus containing 1 μ M Thiazovivin. Cells were maintained at 37°C, 5% CO₂ throughout the six-day protocol. 24 h following cell seeding (D0), cells were rinsed in DMEM/F12. For the undifferentiated H1 control wells, mTESR plus media was replaced for an additional 2 days. After an additional 2 days (day 3 post seeding), undifferentiated H1 cells were lysed using Lysis buffer from the Zymo Quick-RNA Microprep Kit (Zymo R1051).

For anterior and posterior endoderm differentiation, the protocol described in Loh and Ang et al. was used.²⁵ For all steps, media was changed every 24 h after a DMEM/F12 rinse. 1 mL of commercial media A was added to each well for primitive streak induction (ThermoFisher Scientific A3062601) and 1 mL of commercial media B was used for definitive endoderm induction (Thermo Fisher A3062601). For days 3–5 anterior foregut induction, CDM2 with 1 μ M of A8301 (Tocris 2939) and 250 nM of LDN193189 was added to the definitive endoderm cells. For days 3–5 posterior endoderm induction, CDM2 composed of 100 ng/mL FGF, 10 ng/mL of BMP, and 3 μ M of CHIR99201 was added to the cells. On day 5, cells were lysed for RNA extraction.

RNA extraction, cDNA generation, and qPCR

RNA was extracted on day 5 using Zymo Quick-RNA Microprep Kit (Zymo R1051). cDNA was made using high-capacity cDNA reverse transcription kit (ThermoFisher Scientific 43-688-13) following the manufacturer's instructions. After cDNA was synthesized, qPCR was run using a 384-well PCR plate (Applied Biosystems 4343370), SensiFAST SYBR Lo-ROX Kit (Bioline 94050), and respective primers (Table S2) following manufacture's recommended protocol.

Spatial patterning of stem cell differentiation in microfluidic channels

Microfluidic chemotaxis chambers (Ibiditreat μ -slide chemotaxis chambers, Ibidi, Gräfelfing, Germany) were used to establish and maintain a gradient of morphogens across hESCs during anterior foregut and posterior endoderm induction. These microfluidic devices are commercially available, sterile, disposable, and designed to facilitate chemotaxis studies.⁵³ Each device is the size of a microscope slide (2.55 cm \times 7.55 cm) and contains three separated cell culture channels that are supplied with media by larger triangular reservoirs at either side of each cell culture channel (Figure 1B). Prior to cell seeding, the cell culture channels were coated with Geltrex diluted 1:100 in DMEM/F12 media for 2 h at room temperature. Geltrex was introduced to the cell culture channels by manually pipetting following the manufacturer's instructions; 6 μ L of Geltrex was added to the top of a filling port for the central channel, and then drawn through the channel by aspirating from the opposite port. After 2 h, the channels were rinsed in the same way with DMEM/F12 and the devices were maintained at 37°C and 5% CO₂ overnight. For cell seeding, a confluent well of H1 hPSCs was dissociated into single cells using either TrypLE Express (Thermo Fisher 12604039) or Accutase (ThermoFisher 00-4555-56). The dissociated single cells were resuspended to a concentration of 10 million cells/mL in mTESR plus with 1 μ M of ROCK inhibitor Thiazovivin (Tocris 3845). CDM2 basal medium was composed of 50% IMDM (Gibco 31980-097), 50% F12 (Gibco 31765-092), polyvinyl alcohol (Sigma P8136-250G), concentrated lipids (Gibco 11905-031), monothioglycerol (Sigma M6145), insulin (Roche 1376497), transferrin (Roche 652202), and penicillin/streptomycin (Gibco 15140163).

To seed cells into the devices, 10 μ L of cell suspension was introduced to each of the three cell culture channels of the device. The cells were then left to adhere to the matrix overnight at 37°C and 5% CO₂. The following day, the cells were rinsed once in DMEM/F12 by passing 10 μ L of DMEM/F12 over the cells to remove non-adherent cells and debris. Then, an additional 10 μ L of Geltrex was introduced to each channel and incubated at 37°C for 20 min. Following this, we no longer rinsed the cell culture channel directly through the top and bottom ports.

For primitive streak induction on day 1, commercial media A (ThermoFisher Scientific A3062601), or a cocktail of 100 ng/mL of Activin A for activating TGF β (RD Systems 338-AC-500), 3 μ M of CHIR99021 to activate Wnt (Tocris 4423), 10 ng/mL of FGF2 (PeproTech 100-18B), and 50 nM of PI103 to inhibit PI3K (Tocris 2930) in basal media CDM2, was added to the media reservoirs. For definitive endoderm induction on day 2, the media reservoirs were rinsed with DMEM/F12 and then filled with commercial media B (ThermoFisher Scientific A3062601), or a cocktail of 100 ng/ml of Activin A, 250nM LDN193189 (Tocris 6053) to inhibit BMP, and 50nM of PI103 in basal media CDM2. For days 3–5, the cell culture channels and media reservoirs were rinsed with DMEM/F12. Then,

the left reservoir was filled with anterior foregut induction media, while the right reservoir was filled with posterior endoderm induction media. For anterior foregut induction, CDM2 with an added 1 μM of A8301 (Tocris 2939) TGF β inhibitor and 250nM of LDN193189 was used following Loh and Ang et al.²⁵ For posterior endoderm induction, CDM2 with an added 100 ng/mL FGF2, 10 ng/mL of BMP4, and 3 μM of CHIR99201 was used following Loh and Ang et al.²⁵ Media in each side reservoir was replaced once every 24 h. For rinse steps and to replace the media in each side reservoir, 15 μL of solution was added to the inlet and 15 μL of solution was removed from the outlet of each side reservoir 5–6 times.

Control experiments testing one gradient only were performed using the same protocol up until day 2. From days 3–5, either for definitive endoderm induction. For gradients in anteriorizing signals, only the left reservoir was filled with anterior foregut induction media, while the right reservoir was filled with CDM2 for days 3–5. For gradients in posteriorizing signals, the right reservoir was filled with posterior endoderm induction media, while the left was filled with CDM2 for days 3–5 or 3–6. Media in each side reservoir was replaced every 24 h as above.

Cells were fixed inside the microfluidic chips using 4% paraformaldehyde (Fisher AA433689M) in 1X PBS (Gibco). First, each side reservoir was rinsed six times with 15 μL DMEM/F12. Next 15 μL of 4% PFA was added four times to each side to replace the DMEM/F12. After 15 min at room temperature, each side reservoir was rinsed six times with 15 μL of 1X PBS. The cells were then permeabilized in antibody dilution buffer (ADB), consisting of 1 wt % bovine serum albumin (BSA) and 0.1 v/v% Triton X- in 1X PBS. First, 10 μL ADB was added to the central channel. Next, 15 μL ADB was added to each side reservoir five times. After 1 h, primary antibody solution was prepared following Table S3. Antibodies were diluted in ADB and added to the side reservoirs (15 μL , four times) and the central channel (10 μL , once), taking care to pipette slowly so as not to crumple the fixed sheet of cells due to shear stress. After incubation overnight at 4°C or 3 h at 25°C, the cells were rinsed with 1X PBS (six times 15 μL per side reservoir and once with 10 μL in the central channel). Secondary antibody solution was introduced following the same pipetting scheme described for the primary antibody solution (Table S3) and incubated at 25°C for at least 2 h. Prior to imaging, cells were again rinsed in 1X PBS.

Discrete uniform morphogen concentration experiments

For discrete uniform morphogen concentration experiments, cells were cultured following the protocol outlined in Section 2. hPSCs were seeded onto Geltrex-coated 12-well #1.5 glass-bottom plates (Cellvis), and a media volume of 0.5 mL was added to each well. During the patterning steps, AFG and MHG media were mixed before being added to the wells to recapitulate morphogen concentrations from $t = 24$ h of the COMSOL modeling, at positions $x = 0, 250, 500, 750,$ and $1000 \mu\text{m}$. In addition, positive controls that exposed cells to AFG and MHG media for days 3–5 were performed. Following patterning, cells were fixed using 4% PFA and immunostained for Hoechst, FOXA2, OTX2, and CDX2 as described above.

Modeling concentration gradient profiles and dynamics

Distributions of extracellular signals across the cell culture channels were modeled using the numerical simulation software COMSOL Multiphysics. For proteins FGF2 and BMP4, the reported molecular weight as determined by SDS-PAGE in non-reducing conditions was used. Hydrodynamic radii were estimated by assuming an average protein density of 1.35 g/cm^3 and determining the minimum radius required to contain the mass of the protein molecule.⁶⁴ To estimate the diffusion coefficients for small molecules A8301, LDN193189, and CHIR99021, the Stokes–Einstein equation was used.⁶⁵ To estimate the diffusion coefficient for proteins, an empirical correlation derived by He et al. was used. The resulting diffusion coefficients were as follows: $D_{\text{A8301}} = 6.20 \times 10^{-10} \text{ m}^2/\text{s}$, $D_{\text{LDN193189}} = 5.94 \times 10^{-10} \text{ m}^2/\text{s}$, $D_{\text{FGF2}} = 9.26 \times 10^{-11} \text{ m}^2/\text{s}$, $D_{\text{BMP4}} = 6.94 \times 10^{-11} \text{ m}^2/\text{s}$, $D_{\text{CHIR99021}} = 5.99 \times 10^{-10} \text{ m}^2/\text{s}$. For all simulations, ambient temperature was set to 37°C, and the physical properties of water were assumed, with the exception of viscosity, where that of cell culture media was used ($0.78 \times 10^{-3} \text{ N s m}^{-2}$ at 37°C).⁶⁶ The model did not consider chemical degradation, morphogen-morphogen interactions, or morphogen-Geltrex interactions.

To model the morphogen gradient dynamics within the microfluidic devices, the side reservoir and cell channel geometries were rendered in 3D. No-flux boundary conditions were applied to all surfaces, excluding the interfaces between the side reservoirs and central cell culture channel. Initial concentrations of all extracellular signals in the AFG and MHG media were set in the left and right reservoirs, and a time-dependent simulation for transport of dilute species was performed for 0–24 h. The graphs in Figure 1C represent the concentration profile along a line passing through the center of the cell culture channel, 35 μm above the bottom of the channel, and shows the establishment of the gradient in both directions over the course of 24 h. The gradients stabilize by approximately 2 h and remain stable over the course of 24 h.

Experiments testing the ability of the microfluidics to generate and maintain linear gradients were performed using solutions of fluorescein (F6377-100G, Sigma Aldrich, Burlington, MA) (Figures S4B and S4C). Following manufacturer's instructions, several devices were filled such that the right reservoir had a concentration of 10 μM , while the left had a concentration of 50.5 μM . Fluorescein gradient measurements within the microfluidic chambers were performed using inverted Zeiss LSM780 and LSM880 multiphoton laser scanning confocal microscopes equipped with 63x oil/1.4 NA Plan-APO objectives. For optimal optical sectioning, the pinhole was set to 1 Airy Unit, and Nyquist optimal image size and pixel dwell time yielded a pixel size of $0.0852 \mu\text{m}^2$. Tiled images were collected to reconstruct a full view of the device channel and portions of both side reservoirs. The argon laser line 488 nm and standard filter set was used for fluorescein excitation. For each time point, fluorescein emission and transmitted light images were collected for three replicate channels at 3–4 positions along each channel.

Analysis of the fluorescein gradients was conducted as previously described (Zengel P et al. BMC Cell Biology 2011), with some modifications. Briefly, a blank subtraction for autofluorescence of the Ibidi chemotaxis chamber was conducted in FIJI based on a negative imaging control experiment. Then, vertically averaged line traces across the chamber were conducted using a custom python script. Intensities were normalized respective to each image. Curves were aligned based on their global minimum point, corresponding to the left edge of the channel.

In situ hybridization chain reaction for detecting mRNA expression

mRNA expression within patterned cultures in the microfluidic devices was detected using *in situ* hybridization chain reaction version 3.0 (HCR v3.0).⁶⁷ HCR probes, amplifiers, and probe hybridization buffers were purchased from Molecular Instruments (Los Angeles, CA). The microfluidic channels were first rinsed in DBPS and then the cells were fixed in 4% formaldehyde at ~25°C for 10 min. The channels were gently rinsed again in DBPS and cells were permeabilized in 70% ethanol overnight at -20°C. After draining and drying the channels, the cells were rinsed with saline citrate buffer (SSC), incubated in probe hybridization buffer at 37°C for 30 min, and finally incubated in a probe solution containing FOXA2, OTX2, and CDX2 probes in hybridization buffer overnight at 37°C. Next, the cells were incubated in probe wash buffer for 5 min at 37°C, SSC with 1% Tween for 10 min at ~25°C, and amplification buffer for 30 min at ~25°C. The hairpins h1 and h2 were heated to 95°C for 90 s and cooled to ~25°C by placing them in a dark drawer for 30 min. Then the snap-cooled hairpins in amplification buffer were added to cells for overnight staining at ~25°C in the dark. Excess hairpins were removed by washing in SSC containing 0.1% Tween, and antifade mounting reagent was added to the reservoirs of the device. The antifade mounting reagent was too viscous to pass through the central cell culture channel of the device. Notably, the above multiple rinse steps resulted in minor crumpling of cell sheets within the microfluidic devices, but areas of the cell sheets sufficiently large for imaging were preserved.

In situ staining of whole mouse embryos

Outbred CD-1 mice were mated to generate timed pregnancies. Noon on the day a vaginal plug was detected was designated as embryonic day 0.5 (E0.5). Whole embryos were dissected at embryonic day 9.5 (E9.5). Dissections were performed in paraformaldehyde (diluted to 4% in PBS) and fixation was performed in the same solution overnight at 4°C. Following fixation, embryos were washed in PBS with 0.1% Tween 20 (PBST) and dehydrated with graded methanol washes (25%, 50%, 75%, and 100% methanol in PBST). After washing, embryos were stored in 100% methanol at -20°C. Subsequently, whole mount *in situ* hybridization was performed using hybridization chain reaction v3.0 (HCR3)⁶⁷ following the manufacturer's instructions (MI-Protocol-RNAFISH-Mouse, Molecular Instruments). All mouse experiments were performed using procedures institutionally approved by Stanford Administrative Panel on Laboratory Animal Care (APLAC).

Single cell RNA sequencing (scRNAseq) of spatially patterned cultures

To identify the cell types present within the patterned cultures, scRNAseq was performed on cells recovered from six separate cell culture channels after day 5 of differentiation. First, reservoirs at either side of the channel were drained using a pipette. To dissociate cells from the microfluidic chip, Accutase was added at 37°C for 5 min. The device was examined under the microscope to check for cell detachment from the central channel before Accutase was quenched in DMEM/F12. The following steps were adapted from the 10X Genomics Single Cell Protocols.

After dissociation, the cell suspension was strained through a single cell strainer and centrifuged at 500 rcf for 5 min. Dead cells were filtered out using the Miltenyi MACS Dead Cell Removal Kit (Miltenyi Biotech, Gaithersburg, MD), and the live cells were centrifuged again at 500 rcf for 5 min. The binding buffer that remained from the dead cell removal process was gently removed, and the remaining cells were resuspended in DMEM/F12. An automated cell counter (TC20, Bio-Rad, Hercules, California) was used to count the cells, which were later centrifuged at 500 rcf for 5 min. The supernatant was gently aspirated with a pipette and replaced with DMEM/F12 containing 10% Fetal Bovine Serum to reach a total volume of 50 μ L.

Cells were sent to the Stanford Genomics Core for sequencing and a library was prepared using the 10x Chromium Single Cell 3' v3.1 NextGEM system. Data was further analyzed using Seurat v3.⁶⁸

Imaging and image analysis

Imaging of fixed cells in microfluidic devices with countervailing morphogen gradients was performed on an inverted Zeiss LSM 780 laser scanning confocal microscope with Zen Black software to collect tiled z stack 16-bit images. The 405 nm, 488 nm, 561 nm, and 639 nm laser lines with an EC Plan Neo 10x/0.3 numerical aperture (NA) air objective or a Plan Apo 20x/0.8 NA air objective were used to image each fluorescent channel. The pinhole was set to 1 Airy Unit for each emission wavelength. Confocal images of differentiated cells stained for Hoechst, FOXA2, OTX2, and CDX2 were analyzed using custom software written in MATLAB (MathWorks). First, tiled images were stitched in Zen Blue. Then, Fiji was used to sum intensities from all confocal z-slices for each image stack and to remove the brightest pixels.⁶⁹ Next, in MATLAB the Hoechst channel of each image was segmented based on a distance transform followed by a watershed transform, and each resulting object that met nucleus-like criteria for size, solidity, and location within the image was saved as a single nucleus. Then, using the same segmentation, the mean and summed intensities of the nuclei in the FOXA2, OTX2 and CDX2 channels were computed and stored for further processing. For each image, a rectangular region containing nuclei throughout and spanning the width of the cell culture channel was selected for analysis to avoid edge effects. All intensity values were

first normalized to Hoechst to account for differences in cell density, then normalized to the highest FOXA2, OTX2, or CDX2 intensity after any outliers more than three standard deviations outside the mean were removed to account for any variation between imaging sessions. Additionally, blank Ibidi Chemotaxis Chambers were imaged under similar low NA imaging conditions to confirm negligible autofluorescence contributions. To generate the average intensity vs. position plots in Figure 1F, binning was performed for every 50 μm wide strip across the cell culture channel, for a total of 20 bins. This procedure was completed for every replicate ($n = 13$ for OTX2, $n = 15$ for CDX2), then the average and standard error of the mean were calculated for the final plot. Only cells whose centroids fell within the range $x = 0$ to $1000 \mu\text{m}$ were included.

To generate the scatterplots in Figures 1G and 1H, doubly normalized CDX2 vs. OTX2 intensities were plotted for each cell from all replicates. For discrete concentration experiments, $n = 3$ images were taken for each condition and the results were pooled to make up each cluster within Figure 1H. After normalization to Hoechst, cell intensities were again normalized to the highest intensity among the discrete concentration and positive controls.

Fixed cells within microfluidic channels that were subjected to single morphogen gradients were imaged on a laser scanning confocal Zeiss LSM980 microscope. The microscope incubation chamber was always fully closed during imaging to prevent air fluctuation-mediated drift. Confocal images were taken with a Plan-APO 10x/0.45 NA air objective in frame mode. Images were acquired using the Zen Blue software. Master gain was adjusted iteratively in the range of 600–750 values with laser power to fill the dynamic range. The 405, 488, 561, and 639 nm laser lines were used to excite Hoechst, AF488, AF555, and AF647, respectively. The excitation and emission for each channel was separated with a filter set combination containing a beam splitter MBS 488/561/639. Quadruple channel, 5-slice z stack, tile 16-bit images were acquired sequentially and tile-by-tile with bidirectional laser scanning and averaging of 2. Nyquist sampling was used to obtain the optimal lateral pixel size of $0.33 \mu\text{m}$. A z stack was collected to help account for axial chromatic aberration between channels. The pinhole was set to 1 Airy Unit for each channel.

Information theory calculations

All calculations were performed using OTX2 and CDX2 intensities that had undergone normalization and outlier removal as described above, and data from all replicates were pooled. Custom code was written in MATLAB.

The conditional joint distribution $p(\text{CDX2}, \text{OTX2}|x)$ of protein expression levels at a given position was approximated by a bivariate Gaussian distribution. Parameters of the conditional distribution were fit for 20 bins of position and linearly interpolated over the range $x = 0$ to $1000 \mu\text{m}$. This conditional joint distribution was used to compute decoding maps according to Equation 1.⁵⁰ Grayscale intensities in Figures 3D–3F represent normalized probability density.

Decoding map $p(x|x^*)$

$$p(x^*|x) = \int_{-\infty}^{\infty} \int_{-\infty}^{\infty} d\text{OTX2} d\text{CDX2} p(\text{CDX2}, \text{OTX2}|x^*) \cdot \frac{1}{p(\text{CDX2}, \text{OTX2})} p(\text{CDX2}, \text{OTX2}|x) \quad (\text{Equation 1})$$

The channel capacity was computed using the discrete Blahut-Arimoto algorithm as previously implemented (<https://gist.github.com/Piyush3dB/01df75af9889414de1b6>), with 100×100 discrete bins of CDX2 and OTX2 expression obtained from the Gaussian approximation and 100 bins of position x .

The mutual information was computed from the conditional joint distribution assuming a naive uniform prior on the position x [$p(x) = 1$], according to Equation 2:

Mutual information $MI(\text{CDX2}, \text{OTX2}; x)$

$$MI(\text{CDX2}, \text{OTX2}; x) = \int_{-\infty}^{\infty} \int_{-\infty}^{\infty} \int_0^1 dx d\text{OTX2} d\text{CDX2} p(\text{CDX2}, \text{OTX2}|x) \cdot \log_2 \left(\frac{p(\text{CDX2}, \text{OTX2}|x)}{p(\text{CDX2}, \text{OTX2})} \right) \quad (\text{Equation 2})$$

For the individual calculation of single-gene decoding maps and mutual information, Equations 3 and 4 were used.

Single-gene decoding map $p(x|x^*)$

$$p(x^*|x) = \int_{-\infty}^{\infty} d\text{OTX2} p(\text{OTX2}|x^*) \cdot \frac{1}{p(\text{OTX2})} p(\text{OTX2}|x) \quad (\text{Equation 3})$$

$$p(x^*|x) = \int_{-\infty}^{\infty} d\text{CDX2} p(\text{CDX2}|x^*) \cdot \frac{1}{p(\text{CDX2})} p(\text{CDX2}|x)$$

Single gene mutual information $MI(OTX2; x)$, $MI(CDX2; x)$

$$MI(OTX2; x) = \int_{-\infty}^{\infty} \int_0^1 dx \, dOTX2 \, p(OTX2|x) \cdot \log_2 \left(\frac{p(OTX2|x)}{p(OTX2)} \right)$$
$$MI(CDX2; x) = \int_{-\infty}^{\infty} \int_0^1 dx \, dCDX2 \, p(CDX2|x) \cdot \log_2 \left(\frac{p(CDX2|x)}{p(CDX2)} \right)$$

(Equation 4)

Comparing *in vitro* vs. *in vivo* hepatocytes using single-cell RNA-sequencing

To compare the transcriptional similarity between hPSC-derived AFG and E8.75 mouse AFG and between hPSC-derived MHG and E8.75 mouse MHG, the average expression of each gene in the SCTransformed object was calculated using the “AverageExpression” function in Seurat 4.0.4. For the calculation of module scores, the “AddmoduleScore” function in Seurat 4.0.4 was used. The AFG and MHF markers used were based on markers with known expression in the AFG and MHG regions (Loh and Ang et al., 2014). The AFG-enriched markers used to calculate module score are as follows: OTX2, IRX1, IRX3, IRX5, SHISA2, TBX1, SOX2, PAX1, PAX9, NKX2-3, and HESX1. The MHG markers used to calculate module score include: CDX1, CDX2, CDX4, HOXB3, HOXD3, HOXB4, HOXB5, HOXB6, HOXB8, HOXB9, HOXC4, HOXA5, HOXC5, HOXC6, HOXA7, HOXB7, HOXB8, HOXB9, HOXA10, and HOXB6.

QUANTIFICATION AND STATISTICAL ANALYSIS

Confocal images of differentiated cells stained for Hoechst, FOXA2, OTX2, and CDX2 were analyzed using custom software written in MATLAB (MathWorks). First, tiled images were stitched in Zen Blue. Then, Fiji was used to sum intensities from all confocal z-slices for each image stack and to remove the brightest pixels.⁶⁹ Next, in MATLAB the Hoechst channel of each image was segmented based on a distance transform followed by a watershed transform, and each resulting object that met nucleus-like criteria for size, solidity, and location within the image was saved as a single nucleus. Then, using the same segmentation, the mean and summed intensities of the nuclei in the FOXA2, OTX2 and CDX2 channels were computed and stored for further processing. For each image, a rectangular region containing nuclei throughout and spanning the width of the cell culture channel was selected for analysis to avoid edge effects. All intensity values were first normalized to Hoechst to account for differences in cell density, then normalized to the highest FOXA2, OTX2, or CDX2 intensity after any outliers more than three standard deviations outside the mean were removed to account for any variation between imaging sessions. To generate the average intensity vs. position plots in Figure 1F, binning was performed for every 50 μm wide strip across the cell culture channel, for a total of 20 bins. This procedure was completed for every replicate ($n = 13$ for OTX2, $n = 15$ for CDX2), then the average and standard error of the mean were calculated for the final plot. Only cells whose centroids fell within the range $x = 0$ to 1000 μm were included.

To generate the scatterplots in Figures 1G and 1H, doubly normalized CDX2 vs. OTX2 intensities were plotted for each cell from all replicates. For discrete concentration experiments, $n = 3$ images were taken for each condition and the results were pooled to make up each cluster within Figure 1H. After normalization to Hoechst, cell intensities were again normalized to the highest intensity among the discrete concentration and positive controls. Statistical details can be found in subsection 9 of the [method details](#) and in the legend of Figure 1.

scRNAseq was performed on cells recovered from six separate cell culture channels ($N = 6$) after day 5 of differentiation. Cells were sent to the Stanford Genomics Core for sequencing and a library was prepared using the 10x Chromium Single Cell 3' v3.1 NextGEM system. Data was further analyzed using Seurat v3. Statistical details can be found in subsection 8 of the [method details](#).

For qPCR of AFG or MHG cells on days 0, 3, 4, and 5 of the differentiation protocol, $N = 4$ wells of a 12-well plate, error bars = SEM. (Figure S1C). These details are also provided in and in the figure caption.

For experiments testing the ability of the microfluidics to generate and maintain linear gradient fluorescein emission and transmitted light images were collected for three replicate channels ($N = 3$), for each time point, at 3–4 positions along each channel (Figures S4B and S4C). Error bars in Figure S4C represent SEM. These details are also provided in the figure legend.

Distributions of extracellular signals across the cell culture channels were modeled using the numerical simulation software COMSOL Multiphysics.

ADDITIONAL RESOURCES

A document titled “[supplemental information](#)” provides [Figures S1–S7](#), figure legends, [Tables S1–S3](#), and Reaction Diffusion Modeling.